

Rapid and High-resolution Imaging of Lumpectomy Margins Using Deep Ultraviolet Fluorescence Scanning Microscopy

Tongtong Lu

Marquette University and Medical college of Wisconsin

Julie M Jorns

Froedtert and the Medical College of Wisconsin Froedtert Hospital

Mollie Patton

Medical College of Wisconsin

Renee Fisher

Marquette University

Amanda Emmrich

Froedtert and the Medical College of Wisconsin

Todd Doehring

Abemis, LLC

Taly Gilat-Schmidt

Marquette University and Medical College of Wisconsin

Dong Hye Ye

Marquette University

Tina Yen

Froedtert and the Medical College of Wisconsin

Bing Yu (✉ bing.yu@marquette.edu)

Research article

Keywords: Breast-conserving surgery, tumor margin, fluorescence imaging, ultraviolet

Posted Date: February 19th, 2020

DOI: <https://doi.org/10.21203/rs.2.23934/v1>

License:   This work is licensed under a Creative Commons Attribution 4.0 International License.

[Read Full License](#)

Abstract

Background: Re-excision rates for women with invasive breast cancer undergoing breast conserving surgery (BCS or lumpectomy) have decreased in the past decade but remain substantial. This is mainly due to the inability to efficiently and accurately assess the entire surface of an excised lumpectomy specimen during surgery. To address this problem, a deep-ultraviolet scanning fluorescence microscope (DUV-FSM) imaging system was developed and evaluated to determine whether it could accurately detect cancer cells on the surface of excised breast tissue.

Methods: 37 (22 malignant and 15 normal/benign) fresh breast tissue samples of variable size were stained in propidium iodide and eosin Y solutions. A set of fluorescence images were obtained from one side of each sample using low magnification (4x) and fully automated scanning. The images from each sample were stitched to form a color image. Routine histopathology was performed on each sample. Three non-medical inspectors were trained to interpret and assess the fluorescence images. Patch-level nuclear-cytoplasm ratio (N/C) was calculated and ROC analysis with the Youden index was used for tissue classification.

Results: DUV-FSM images a breast sample with subcellular resolution at a speed of 1.0 minute/cm². DUV images show excellent visual contrast in color, tissue texture, cell density and shape between invasive lobular carcinoma (ILC), invasive ductal carcinoma (IDC) and their normal counterparts. Visual interpretation of DUV images was able to distinguish invasive carcinoma from normal/benign samples with high sensitivity (95%) and specificity (94.4%). Pairwise comparison of patch-level N/C identified significant differences ($p < 0.001$) between normal and malignant samples. Using N/C alone was able to differentiate invasive carcinoma from normal breast tissues at the patch-level, with reasonable sensitivity (81.3%) and specificity (79.2%).

Conclusions: DUV-FSM is a simple device that can rapidly image large, unprocessed breast specimens with subcellular resolution and excellent contrast which allows either visual or quantitative detection of invasive cancer cells on the surfaces of a surgical specimen. This study supports further investigation into whether this technology can be used for intraoperative assessment of surgical margins during BCS procedures.

Background

Breast cancer afflicts millions of women in the U.S. and worldwide, of whom about a half to two-thirds will undergo breast conserving surgery (BCS) or lumpectomy.^[1, 2] The goal of BCS is to completely remove the tumor with a narrow rim/margin of normal, unaffected breast tissue while preserving as much normal tissue as possible. Although outcomes have improved over the last decade, women with positive margins (cancer cells at the surface of the surgical specimen) still have at least a 2-fold increased risk of cancer recurrence,^[3-5] and thus, are often recommended to undergo additional surgery to achieve clear margins. Additional surgery is associated with additional discomfort, surgical complications, worse

cosmesis, and additional emotional stress, time and financial burdens to patients and their caregivers.^[6, 7] The current re-excision rate of BCS in the U.S. is 14–18% and highly variable among surgeons, ranging from 0–92%.^[2, 8–11] One reason why women with positive margins need to undergo re-excision surgery is that definitive pathologic margin status is typically not available until several days after surgery.

Currently there are several different methods for intraoperative margin assessment which vary markedly in performance among studies. Radiologic examination of the resected specimen with 2D mammography is largely available and rapid. However, it has low sensitivity and variable accuracy compared to other techniques and does not improve re-excision rates.^[12, 13] Pilot studies evaluating intraoperative specimen radiograph using digital breast tomosynthesis may be promising (sensitivity 77%-93%, specificity 78%-98%) but it requires further investigation.^[14, 15] Frozen section analysis is an involved pathological technique that typically samples only a portion of the surgical margin, performs poorly on fatty breast tissue, and has variable false-negative rates.^[16] In addition, this technique is extremely labor- and time-intensive, costly, requires on-site or telepathology and significantly lengthens operating room (O.R.) time (20–30 minutes).^[13] Cytologic imprint prep analysis by touch preparation or scrape preparation is less labor-intensive (about 13 minutes); however, this technique requires a specialized cytopathologist.^[17] A considerable number of patients undergo BCS at an ambulatory surgery center where there is no pathologist or cytopathologist available. For these reasons, intraoperative pathology options are not routinely available or adopted.^[13, 18] Lastly, the only FDA-approved device for margin analysis, the MarginProbe, is a pen-like probe that utilizes radiofrequency spectroscopy to analyze tumor margins.^[19] Limitations include low sensitivity (75.2%) and specificity (46.4%) and reliance on user-guided spot scanning.

Margins of resected lumpectomy specimens have recently been assessed using a number of emerging technologies, including optical coherence tomography (OCT),^[20–23] diffuse reflectance spectroscopy (DRS),^[24–26] DRS and fluorescence spectroscopy,^[27] Raman spectroscopy,^[28] photoacoustic tomography (PAT),^[29–31] fluorescence or polarization imaging,^[32, 33] spatial frequency domain imaging (SFDI) or structured illumination imaging,^[34, 35] bioimpedance spectroscopy (ClearEdge),^[36] mass spectrometry (i-Knife),^[37] light-sheet microscopy,^[38, 39] among others. A detail review of these emerging techniques can be found in two recent comprehensive reviews.^[40, 41] While each of these studies has shown promising results, none of the emerging imaging technologies has demonstrated the capability of analyzing an entire lumpectomy specimen (six margins) with both adequate microscopic resolution and time efficiency required in a clinical setting.

Microscopy with UV surface excitation (MUSE) is a novel, nondestructive technology that can image fresh, unfixed tissue that is stained with multiple fluorescence dyes, thus generating fluorescence images with outstanding resolution, sharpness and contrast.^[42] Yoshitake et al.,^[43] found that the histological features of breast tissue images obtained with a high incident angle water immersion illumination MUSE system have limited correspondence with those obtained with conventional hematoxylin and eosin (H&E) histology, and suggested that further development is needed for breast surgical applications. Xie et al.

developed a MUSE system with a fully automated 3-D sample translation that can image fresh tissue at a rate of 5 min/cm², and an algorithm that can create a fluorescent analog of conventional H&E images. They further demonstrated that MUSE could provide microscopic visualization of breast margin surfaces at speeds relevant for intraoperative use.^[44]

In this study, we investigated the translational potential of MUSE as an intraoperative tool for margin assessment during BCS. Specifically, we aimed to determine the features of MUSE images that can be used to distinguish fresh, unprocessed malignant from normal/benign breast tissues; the accuracy of the technology; and the speed a lumpectomy specimen can be surveyed. We demonstrate that: 1) a low-cost deep-ultraviolet fluorescence scanning microscope (DUV-FSM) can rapidly image (1.0 cm²/min) fresh breast tissues at a subcellular resolution with excellent contrast; 2) visual interpretation of DUV images can achieve excellent sensitivity and specificity in detecting invasive samples; and 3) nuclear-cytoplasm ratio (N/C) may also be used for quantitative assessment of margin status.

Methods

Imaging system

We have converted an inverted microscope to a DUV-FSM to image the surfaces of fresh tissues from breast surgical specimens. A schematic of the DUV-FSM system is shown in Figure 1. A 285 nm LED (M285L4, Thorlabs, Newton, NJ) is mounted on the right side of an inverted fluorescence microscope (EXI-310, Accu-scope, Commack, NY) for oblique back-illumination. A 325 nm short-pass filter (XUV0325, Asahi Spectra, Torrance, CA) is placed in front of the LED to block emission spectrum tails in the visible range, avoiding possible overlap with fluorescence signals. A fused silica ball lens (model #67-388, Edmund Optics, Barrington, NJ) is used as a condenser to converge the LED radiation for a smaller illumination field and improved power density. The LED, short pass filter and ball lens are mounted inside a lens tube. A 3D printed arm holds the lens tube and is mounted on an optical post to allow for easy adjustment of the LED height and illumination angle so that the illumination area is slightly larger than the field-of-view (FOV) of the 4x microscope objective. Once the position of the LED was optimized, the entire system was fixed on an optical breadboard. To image a lumpectomy specimen, the specimen is placed on one of its six margins in a 70 mm diameter quartz dish to minimize autofluorescence of the glass. The quartz dish is mounted on a robotic, stepper-motor controlled XY stage custom designed for fast mosaic imaging (ABĒMIS LLC, Cleveland, OH). The excitation/emission filter block of the microscope is switched to the empty position so that the fluorescent signals of multiple fluorophores can be captured by a color camera without having to switch emission filters during the imaging process. A cooled, USB3.0 camera (MTR3CCD06000KPA, Hangzhou ToupTek Photonics Co., Ltd, Hangzhou, China) was selected for its large image sensor and pixel size, very low dark noise, and high image transfer speed, which are very important for fast image acquisition in intraoperative margin assessment. The camera has 2748 × 2200 pixels, pixel size of 4.54 μm and active area of 14.6 × 12.8 mm². A 4x apochromatic long working distance objective lens with a numerical aperture of 0.13 was selected as a compromise between good lateral resolution (2~3 μm) and a large effective imaging area of 3.48 x 2.78 mm. The FOV of the

objective lens is slightly larger than the imaging area of the camera to avoid distortions at the edge of the FOV. The microscope is housed inside a dark enclosure to prevent personnel exposure to DUV light and to eliminate background from room light.

Figure 1 The DUV-FSM margin imaging system: (A) Principle schematic of the system and (B) The simplified imaging light path. A 45 mW, 285 nm LED with a short-pass filter and a fused silica ball lens has been added to the inverted fluorescence microscope for fluorescence excitation. Fluorescence emission is collected by a Plan Fluor 4x (numerical aperture = 0.13) objective. The excitation/emission filter block of the microscope is switched to the empty position. Large specimen mosaic scanning is achieved by a motorized XY stage.

Breast tissue sample preparation

Thirty-seven fresh human breast tissues obtained from both lumpectomy and mastectomy specimens were acquired from the Medical College of Wisconsin (MCW) Tissue Bank. Information about the tissue subtype, number of samples, and surface area are provided in Table 1. Specimens were grossly examined and procured by Tissue Bank staff (MP), then placed in phosphate-buffered saline (PBS) solution, transported on ice to the research lab immediately, and stored in a refrigerator. Samples were imaged during the same day of excision. Propidium iodide (PI, P21493, Thermo Fisher Scientific, Waltham, MA) was used for nuclear staining and eosin Y (EY, 230251-25G, Sigma-Aldrich, St. Louis, MO) for staining of cytoplasm and connective tissues. Both PI and EY can be effectively excited at 285 nm. PI has a fluorescence emission in the yellow-red spectral range and EY has an emission in the green-yellow spectral range. For staining, PI and EY were dissolved in PBS (pH 7.2) to a concentration of 100 µg/ml and 1.0 mg/ml, respectively. Each specimen was stained in the PI solution for 1 minute, then in the EY solution for 20 seconds, and finally rinsed in PBS for 10 seconds. Once staining was completed, the specimen was placed onto the quartz plate of the specimen holder. A wide pallet knife was used to gently flatten the tissue against the quartz plate to remove air bubbles between the tissue and plate. Once the tissue was in the correct position, excess liquid was removed from the edges using a Kimwipe.

Table 1 Tissue types, number of samples, surface area, and number of patches (2 mm × 2 mm)

Tissue type	No. of Samples	Surface Area (cm ²) (Median)	Patches/Sample (Median)	Total Patches
IDC	18	0.44 - 5.5 (1.3)	3 - 48 (19)	358
ILC	4	2 - 3.9 (2.8)	4 - 55 (15.5)	90
Adipose-rich Normal	3	3.9 - 5.29 (4.8)	48 - 70 (58)	176
Fibrous/Glandular-rich Normal	12	2.4 - 9 (4.4)	36 - 141 (84)	1,005

Imaging protocol

The specimen holder loaded with a tissue specimen was immobilized on the motorized XY stage after a specimen size measurement by a caliper. The focal plane was set at the bottom surface of the specimen. Mosaic images were collected with conservative overlapping regions of 0.75 mm in the X direction and 0.60 mm in the Y direction for a tradeoff between speed and stitching accuracy. The number of scanning steps are decided by the specimen size, effective imaging area and overlapping region dimension. The temperature of the camera was set to -18 °C to reduce the electronic noise level. All images of each specimen were captured with a constant exposure time ranging from 50 to 100 ms, depending on the sample tissue type. The image acquisition and motor movements were controlled by a customized software developed in Microsoft Visual C# .NET. Image files were saved in TIFF format with 2748 x 2200 pixels. After imaging, the raw images were transformed to hue-saturation-lightness (HSV) color space images. The open source image processing package Fiji (fiji.sc/) was used to process the tissue images. A Fiji plugin named BaSiC ^[45] was applied to the saturation and lightness channels to correct for background and shadings caused by uneven and tilted illumination. The color space transform is necessary to preserve the original color information during illumination correction. After transforming back to red-green-blue (RGB) color space, image stitching was performed using a Fiji plugin developed by Preibisch et al.^[46] Lastly, histogram equalization was applied to the R and G color channels of the stitched image to enhance the visual contrast.

Histopathology evaluation

Routine histopathology was used for final diagnosis of the tissue samples. Fereidouni et al. has previously shown PI and EY staining does not interfere with downstream histopathology processes.^[42] Following DUV-FSM imaging, tissue specimens were returned to MCW Tissue Bank for formalin-fixed paraffin-embedded (FFPE) tissue processing. In order to obtain full face sections for histologic evaluation, an average cut depth of ~200 µm into the embedded tissue block was used during microtomy. The tissue sections were transferred to glass slides and stained with H&E. All slides were digitalized by a Panoramic 250 Flash II slide scanner (3DHistech Ltd., Budapest, Hungary). An unblinded qualitative side by side comparison of the H&E and DUV-FSM images was performed by an experienced breast pathologist (JMJ).

Visual inspection of DUV images

Visual inspection of DUV images was performed by three trained non-pathologists to evaluate the accuracy of non-pathologists to differentiate cancer from non-cancer tissue. The 37 breast tissue samples were divided into two groups: a training and a test group. The training group included 3 invasive carcinomas (2 IDC and 1 ILC) and 2 normal tissues (1 fibrotic and 1 adipose-rich breast sample), while the test set included 3 ILC, 16 IDC, 2 adipose-rich and 11 non-adipose-rich normal samples. Three non-medical inspectors (TGS, DHY and AE) who were blinded to pathological diagnosis were trained by the pathologist (JMJ) and imaging engineer (TL) during a one-hour session to visually identify the diagnostically useful features (such as adipose, ducts, cell density, infiltration, etc.) in the training DUV images using the associated H&E images. After training, each inspector was provided DUV images of

samples in the test group without access to correlative H&E images. The inspectors interpreted DUV images and provided a diagnosis (invasive carcinoma vs. normal) for each of the test samples.

Quantitative image analysis

Quantitative analysis was applied to DUV tissue images to extract diagnostically useful parameters that may be useful for detecting positive tumor margins of lumpectomy specimens during BCS. Previous studies have shown that breast cancer cells have irregular cell size and shape, enlarged nuclei, and increased N/C.^[47, 48] In this study, we investigated the feasibility of using N/C as a biomarker to differentiate invasive carcinoma from normal breast parenchyma at the surface of the tissue samples. Tumor region(s) on the stitched DUV image was outlined based on the corresponding H&E image. Since PI-stained cell nuclei primarily emit lights in the yellow-red wavelength range, only the R-channel of the stitched images in RGB color space was extracted and used to calculate the N/C.

The process for N/C calculation is illustrated in Figure 2. First, the color image (A&E) was converted to a R-channel image (not shown). Segmentation of the R channel image was implemented by combining edge detection and intensity thresholding.^[49] The edge detection Sobel operator with adaptive threshold detects the edge information, while intensity thresholding eliminates textures caused by other features. The intensity threshold was set to 70% of the 1% brightest pixels in the image based on our experience. The segmented full R image (B&F) was divided into a set of small patches of 250 μm x 250 μm (or 198 x 198 pixels) in size, and N/C was calculated for each small patch (C&G). Then, N/Cs of neighboring 8 x 8 small patches were averaged and merged to form a large patch of 2 mm x 2 mm in size (D&H). Larger patches were used to reduce the sensitivity to small features, such as lobules, ducts and blood vessels. In general, larger patch size results in lower spatial resolution and sensitivity for cancer cell detection, but also lower false positive rate. To minimize the effect of tissue patches at the boundaries, large patches with more than half (or 32) small patches that have no cells (i.e., N/C = 0) were excluded in further analysis. A window size of 2 mm x 2 mm was selected to match the spatial resolution of standard breast pathology which samples at a step of 2 mm.

Figure 2 Demonstration of N/C calculation process with an IDC (A-D) and a normal sample (E-H). (A&E) A 4 mm x 4 mm area from the fluorescence images of an IDC and a normal sample, respectively. (B&F) The binarized image after nuclei segmentation from the same region as in (A&E). (C&G) The N/C image calculated with small patches (250 μm x 250 μm). (D&H) 8 x 8 small patches in (C&G) are binned to form large patches (2 mm x 2 mm).

The large patches were manually classified into adipose-rich, non-adipose-rich normal, ILC and IDC in accordance with H&E images. The number of large patches per tissue sample and total number of patches for each tissue subtype are presented in Table 1. This resulted in a total of 1,629 large patches of N/C images, including 358 patches from 18 IDC, 90 patches from 4 ILC, 176 patches from 3 adipose-rich and 1,005 patches from 12 non-adipose-rich normal tissues. All patches were used for the following comparison and classification studies. The mean N/C was compared between the 4 tissue subtypes (IDC,

ILC, adipose-rich, non-adipose-rich normal groups) and between invasive (IDC, ILC) and normal tissue using Generalized Estimating Equations (GEE) to account for repeated observations per sample. Tukey's adjustment was used for multiple pairwise comparisons.^[50] For classifications, ROC curves were constructed using patch-level N/C to predict invasive versus normal tissue, IDC versus ILC among invasive samples, and adipose-rich versus non-adipose-rich tissue among normal samples. The Youden Index, which weighs false positive and false negative errors equally, was used to determine the cutoff point for the calculation of patch-level sensitivity and specificity in differentiating invasive and normal tissue. The analysis was done using SAS 9.4 (SAS Institute, Cary, NC).

Results

Breast tissue images

The study resulted in stitched DUV images and FFPE H&E images obtained from 37 breast specimens. The average imaging speed was 1.0 minute/cm². DUV fluorescence and H&E images of one sample from each tissue type are presented below. Figures 3(A-F) show fluorescence and H&E images of a sample of benign breast glands with interspersed fibroadipose tissue stroma. Fluorescence images show adipocytes (C) to appear as individual or clusters of rounded small droplets in dark green with hypo-scattered bright pink nuclei at many locations. Loose connective tissue shows low nuclear density and appears mostly green (A). Tubular-shaped structures, e.g., blood vessels (D), ducts (E) and lobules (F and G), are easily identifiable. The two-layers of epithelia of the ductal-lobular system have higher nuclear densities than blood vessels. Terminal duct lobular units (TDLU) exhibit high nuclear density and their shapes are more complicated than ducts and blood vessels. Additionally, lobules (F and G) have clustered foci of dense nuclei comprising glands while ducts (E) tends to have a solitary structure.

Figure 3 Normal human breast tissue. The fluorescence image (A) of a sample (21 mm x 21 mm) of benign breast glands with interspersed fibroadipose tissue stroma with the specimen photo in the white box and corresponding FFPE H&E image (B). The fluorescence images and corresponding H&E images are shown for (C) adipocytes, (D) muscular-walled blood vessel indicated by the red arrow, (E) duct indicated by the blue arrow, (F) small lobule indicated by the yellow arrow, and (G) lobule with mild adenosis and dilated glands indicated by the black arrow.

Fluorescence and H&E images of a grade 1 ILC with multiple foci of DCIS and surrounding adipose tissue are shown in Figure 4. ILC cells in the middle appear in pink and yellow in the DUV fluorescence image (A) and can be easily distinguished from the adipocytes in dark green at the left and the right sides. Tumor regions exhibit infiltrating single cells characteristic of ILC (C). Four DCIS sites were identified in the H&E image (B), three of which (indicated by yellow arrows 1-3) were on the surface and appeared to be dark or have loss of fluorescence in (D, E and F). The shallow penetration depth (~20 μm ^[43]) of DUV lights makes DCIS below the surface invisible, such as the one indicated by arrow 4 in the H&E image. A biopsy site shows higher brightness in yellow with lighter background color (G). The benign adenosis region (H) also has a high nuclear density but lacks single file infiltrating patterns seen in tumor regions. Air bubbles

also appeared in the fluorescence image, but careful specimen handling and flattening can alleviate or avoid such artifacts.

Figure 4 Human breast tissue with ILC and DCIS. (A) The fluorescence image of an ILC sample (20 mm x 10 mm) with adjacent adipose tissue at the two ends. A specimen photo is presented in the white box. (B) FFPE H&E image of the same sample. (C) ILC highlighted by the blue box. Infiltrating single cells and files of cells are evidently visible in the fluorescence image. (D-F) DCIS sites pointed by arrows 1, 2, 3, respectively. The DCIS indicated by arrow 4 is not visible in the fluorescence image, likely because it is slightly below the surface. (G) Biopsy site highlighted by the black box. A biopsy site usually forecasts abnormalities within the site or nearby. (H) Benign adenosis highlighted by the red box.

Fluorescence and H&E images of a grade 2 IDC surrounded by adipose tissue are shown in Figures 5 (A&B). Adipocytes on the left, right and upper sides appear darker in green than the epithelial and connective tissues (A). Like the ILC specimen above, IDC cells in the middle appear in pink and yellow and can be easily distinguished from the adipocytes in dark green and epithelial and connective tissues in light green in (A). The larger, dense ducts indicate this specimen was taken from a location near the nipple. Large branching ducts in the unfixed specimen could have been compressed and show different shapes in the fluorescence image (C, D and E). The tumor area highlighted by the blue box has high nuclear density and is at the interface between fibrotic stroma and adipose tissue (F), which correlates well with the corresponding H&E image. A portion of the upper side of the specimen was compressed during imaging and shows clear folds. A thorough check before imaging can avoid this issue. The fluorescence and H&E images of a high-grade IDC specimen with necrosis and adipose tissues are shown in Figures 5 (G&H), respectively. Again, adipose tissue on the left side appears dark green and the tumor region appears in pink with a high nuclear density of irregular and poorly differentiated cells. Foci of necrosis are observed from the fluorescence image and corresponding positions on the H&E images which show weaker (pink) nuclear staining and loss of cellular detail (I).

Figure 5 Human breast tissues with IDC. (A) The fluorescence image of an IDC sample (25 mm x 18 mm) with 3-sides surrounded by adipose tissues. The specimen photo is presented in the white box. (B) The FFPE H&E image of the same sample. Benign ducts are indicated by red, yellow and black arrows from different sites and their UV and H&E images are shown in (C), (D) and (E), respectively. The tumor site with higher nuclear density at the interface between fibrotic stroma and adipose tissue in the blue box is shown in (F). (G) The fluorescence image of a high-grade IDC sample (25 mm x 17 mm) with necrosis and the specimen photo in the white box. (H) FFPE H&E image of the same sample. The region in the red box is exhibited in (I) with the necrosis sites indicated by the yellow arrows.

Performance of visual interpretation of DUV images

Results from visual interpretation of the DUV images of the 32 tissue samples in the test group by the three inspectors are summarized in Table 2. Inspector A identified all cancer samples correctly, while Inspector B missed one and Inspector C missed 2 (false negative rates of 5-10%). Inspectors A diagnosed two normal samples as cancer (false positive rate = 16.7), but Inspectors B and C identified all normal

samples correctly. Overall, the three inspectors achieved an average sensitivity and specificity of 95% and 94.4%, respectively, and an accuracy of 94.8%. Inspectors spent approximately 1-2 minutes to review the DUV image of a test sample before making a diagnosis.

Table 2. Results of visual diagnosis of the 32 breast samples in the test group.

	Inspector A		Inspector B		Inspector C		Average
	Cancer	Normal	Cancer	Normal	Cancer	Normal	
Path Cancer	20	0	19	1	18	2	
Path Normal	2	10	0	12	0	12	
Sensitivity	100%		95%		90%		95%
Specificity	83.3%		100%		100%		94.4%
Accuracy	93.8%		96.9%		93.8%		94.8%

Quantitative analysis by N/C values

The 1,629 large patches of N/C images from 37 breast tissue samples were manually classified into adipose-rich, non-adipose-rich normal, ILC and IDC tissues in accordance with the H&E images. Figure 6(A) shows the boxplot of N/C per sample of the four tissue types. The calculated mean patch-level N/C value was 0.0280 ± 0.0098 for adipose-rich ($n=176$), 0.0712 ± 0.0064 for non-adipose-rich normal tissues ($n=1,005$), 0.2082 ± 0.0187 for IDC ($n=358$), and 0.2701 ± 0.0599 for ILC ($n=90$). The GEE model determined that there was a significant difference ($p<0.001$) among the 4 tissue subtypes except between ILC and IDC ($p=0.32$). Figure 6(B) shows boxplots of two-class comparison, showing N/C of invasive carcinoma (IDC and ILC) to be significantly different ($n<0.0001$) from normal tissues. In the ROC curve in Figure 6(C), the area under the curve (AUC) was 0.8622 and the patch-level sensitivity and specificity in differentiating invasive carcinoma from normal tissues using N/C alone were determined to be 81.3% and specificity 79.2%, respectively.

Figure 6 Results of statistical comparison and classification. (A) The boxplot of N/C by specimen subtype (adipose-rich, non-adipose-rich normal, IDC and ILC). (B) The boxplot of two-class classification. Outliers are represented by red crosses in (B). (C) ROC curve for classifying patch-level normal and invasive tissue. J is the Youden's index.

Discussion

This study investigated the feasibility of using DUV fluorescence scanning microscopy as a potential intraoperative tool to detect positive margins of freshly excised breast tumor specimen during BCS. Propidium iodide and eosin Y have been used to stain the tissues for enhanced fluorescence contrast between invasive and normal/benign breast tissues. Our DUV images show excellent visual contrast in

color, tissue texture, cell density and shape between ILC, IDC and DCIS and normal tissues. Non-expert researchers with minimal training were able to accurately and quickly distinguish IDC and ILC from normal breast tissues by simple visual interpretation of DUV images. The extracted N/C for invasive carcinoma was significantly different (Fig. 6B) from that of normal tissue. Reasonable patch-level sensitivity and specificity in differentiating invasive carcinoma from normal was achieved by using a trained statistical classification model and N/C as a single discriminator.

DUV-FSM has several important features. First, DUV-FSM can image large margins of variable size with subcellular resolution. Since the size of lumpectomy margins varies and most positive margins typically involve small microscopic foci of cancer,^[51] a device with both large margin coverage and microscopic resolution is highly desirable to rapidly evaluate lumpectomy margin status intraoperatively with both low false-negative and false-positive rates. However, many technologies currently under investigation are either a point device (e.g., optical spectroscopy, i-Knife, MarginProbe) or a high resolution device with very small field of view (e.g., OCT, confocal) that requires excessive time to manually scan a surgical margin, or a wide-field imaging device with very low spatial resolution (e.g., fluorescence imaging, SFDI). Compared to near-infrared light and visible light, using DUV light to detect tumor at the surface should result in much higher spatial resolution ($2 \sim 3 \mu\text{m}$) even with a low magnification objective (e.g., 4x), which is sufficient in resolving cellular structures and cell nuclei in ex vivo breast tissue, and much lower background noise caused by fluorescence emission from deeper cells and tissue scattering. With automated scanning and stitching, lumpectomy margins of different size can be easily surveyed by varying the number of 4x images in the X and Y directions in the user interface of the DUV-FSM software. This feature is clinically critical because it allows tumor margins of a wide range dimensions to be imaged rapidly during BCS.

The DUV-FSM system described here, like other MUSE devices,^[42-44] directly images fresh specimens without the need for complex intraoperative radiography and/or pathology processing. This method is extremely simple, easy to use, relatively low in cost, and does not require radiology, pathology or cytology expertise, thereby making it attractive to community hospitals and surgery centers where most BCS procedures are performed. Using DUV-FSM for intraoperative margin imaging is nondestructive to the specimen and does not negatively impact postoperative pathology, which remains the gold standard for margin assessment. The sensitivity and specificity for rapid visual inspection of DUV images were high, even amongst non-expert inspectors with minimal training, and thus should not pose significant barriers to surgeon adoption or operating room workflow as most surgeons already interpret specimen radiograph results. To our knowledge, this study is the first to report the sensitivity and specificity of MUSE technology for breast margin detection.

Previous MUSE studies focused on creating H&E mimicking images by color mapping for histopathological assessment which requires a pathologist to interpret the images. While creating H&E mimicking images from MUSE images is necessary to understand if MUSE can provide the same or equivalent diagnostically useful information as one can get from routine pathological analysis, it is also important to investigate how this technology may be used in a clinical setting where large and variable

margin coverage, high speed and simplicity are key factors. This DUV-FSM study emphasizes the importance of providing surgeons diagnostically interpretable information about margin status within minutes. We aim to generate high contrast images that allows a surgeon to visually diagnose or a computer algorithm (e.g., statistical or machine learning model) to determine if a margin is positive and re-excision is necessary to achieve a negative margin during the primary surgery. Best efforts are focused on achieving a balance between high resolution to obtain more cellular and subcellular details about the tissue surface and fast scan speed that allows specimen processing, imaging and interpretation of all six margins of a lumpectomy specimen. Using a low 4x magnification objective with a FOV of 4.48 mm in diameter, simultaneous excitation of two fluorescence dyes with distinct emission color (PI and EY), and a USB 3.0 color camera to detect the fluorescence signals significantly reduces the scan time for a large specimen to 1 cm²/min. The DUV-FSM method requires 80 seconds for sample staining and ~ 1 minute for image processing. In contrast, the Xie system requires 5 minutes for staining, 5 minutes to scan a 1.0 cm² margin, and 5 minutes for image processing to create fluorescent analog of H&E staining.^[44] In addition to providing surgeons high contrast images for visual inspection, N/C from DUV images showed significant difference between invasive carcinoma and normal breast tissues and thus it may be used as a complementary biomarker for rapid margin detection during BCS. N/C has not been extensively used as a parameter for intraoperative assessment of breast margins.

This study has some limitations. First, pure DCIS samples were not included in the study. We are aware that the Society of Surgical Oncology (SSO) and American Society for Radiation Oncology (ASTRO) released consensus guidelines on margins in 2016 for BCS with whole breast radiation in the setting of DCIS (with or without microinvasive component), which accounts for about 25% of all breast cancers. The recommendation is to achieve a 2 mm margin to minimize the risk of tumor recurrence in the same breast and emphasizes the importance of clinical judgment in determining selective re-excision for patients with negative margins less than 2 mm.^[52] We acknowledge that DUV-FSM, as well as other MUSE devices, will not be able to assess margins to 2 mm and close margin status (tumor cells present within 2 mm of the surface but not at the surface) will need to be determined on final routine pathological assessment. However, our preliminary work demonstrates the possibility of using DUV-FSM to detect positive margins for DCIS (see Fig. 4D-F), which should translate into decreased re-excision rates in positive-margin cases. Recent data from two large studies showed that women with DCIS who underwent BCS and post-lumpectomy whole breast radiation treatment with a close margin did not have a higher rate of local recurrence compared to those with a wider margin width.^[53, 54] Clasier et al. also concluded that a 2 mm margin may not be necessary if comprehensive surface imaging is achieved.^[38] Therefore, the clinical priority to intraoperatively detect close but negative margins for DCIS cases may decrease in the future.

Second, it was challenging to obtain accurate co-registration between DUV and corresponding H&E images. While DUV fluorescence images were taken from the top 20 µm of samples due to the shallow penetration depth of DUV light, routine H&E slide cutting techniques produces H&E images up to 200 µm deeper into the FFPE tissue block. The optical sectioning thickness of ~ 20 µm is also thicker than a

typical paraffin-embedded thickness of $\sim 4 \mu\text{m}$, which can cause subtle differences between DUV and H&E images. For instance, tubular-shape structures like ducts and blood vessels usually have optically clear lumina in H&E images but this is not the case in fluorescence images (Fig. 3). In Fig. 4A and 4B, one focus of DCIS appears in the H&E image but is not easily identifiable in the fluorescence image. In Fig. 5A, a topology of tissue compression and surface folding, which may be minimum in whole lumpectomy specimens, is visible in the fluorescence image but was not observed in the H&E images.

Ideally, segmentation is expected to accurately segment all nuclei in the background, but this is difficult to achieve with simple edge detection and intensity thresholding because of the complicated textures and nuclei stacking. Fluorescence signals from cells slightly below the specimen surface can cause blurring and reduced intensity in nuclei images due to scattering, thus contributing to error in N/C calculation. A more advanced nuclei segmentation algorithm is needed for more accurate identification of cell nuclei in future studies. Benign structures like adenosis, blood vessels and ducts may also include regions with higher N/C. Given the small size of the vessels and ducts, N/C of these tissue types can be averaged down by using a large patch size. In this study, $2 \times 2 \text{ mm}$ patch size was selected for the calculation of N/C to be compatible with standard histopathology which samplings at a step of 2 mm. An optimal image patch size may be determined by comparing the ROC curves obtained at different patches with more samples.

Finally, the number of breast samples that have been imaged is relatively small. More samples are needed to calculate sensitivity and specificity for detection of positive margins more accurately. It also takes the current DUV-FSM about 1 minute to image a 1 cm^2 breast specimen. Improvements in the motorized XY stage and scanning algorithm, coupled with faster image transfer rate should reduce the scan time by a factor of at least 10. In future studies, DUV images will be used to train a deep learning model for tissue classification which should also further decrease scan time.

Conclusions

In conclusion, a standard inverted microscope has been converted to a DUV-FSM as a potentially promising intraoperative tool for fast imaging of breast margins during BCS. Preliminary fluorescence images show excellent visual contrast in color, tissue texture, cell density and shape between ILC, IDC, DCIS and normal breast tissues. Visual inspection with minimal training achieved excellent accuracy in detecting invasive carcinoma from normal tissues. Statistical analysis identified significant differences in N/C between cancerous and normal tissue and achieved reasonably good sensitivity and specificity. While further work is needed to optimize DUV-FSM, future studies are also needed to explore the potential of DUV-FSM for intraoperative lumpectomy margin assessment.

Abbreviations

2D:2 dimensional; 3D:3 dimensional; ASTRO:American Society for Radiation Oncology; AUC:Area under the curve; BCS:Breast-conserving surgery; DCIS:Ductal carcinoma in situ; DRS:Diffuse reflectance

spectroscopy; DUV:Deep ultraviolet; DUV-FSM:Deep-ultraviolet fluorescence scanning microscopy; EY:Eosin Y; FDA:Food and Drug Administration; FFPE:Formalin-fixed paraffin-embedded; FOV:Field-of-view; GEE:Generalized estimating equations; H&E:Hematoxylin & eosin; HSV:Hue-saturation-lightness color model; IDC:Invasive ductal carcinoma; ILC:Invasive lobular carcinoma; IRB:Institutional review board; LED:Light emitting diode; MCW:Medical College of Wisconsin; MUSE:Microscopy with ultraviolet surface excitation; N/C:Nuclear-cytoplasm ratio; O.R.:Operating room; OCT:Optical coherence tomography; PAT:Photoacoustic tomography; PBS:Phosphate-buffered saline; PI:Propidium iodide; RGB:Red-green-blue color model; ROC:Receiving operating curve; SFDI:Spatial frequency domain imaging; SSO:Society of Surgical Oncology; TDLU:Terminal duct lobular unit; TIFF:Tagged image file format; U.S.:United States.

Declarations

Ethics approval and consent to participate

The study was exempt from the Medical College of Wisconsin / Froedtert Hospital Institutional Review Board #5 (PRO ID: 000032379) and Institutional Biosafety Committee reviews.

Consent for publication

NA

Availability of data and materials

The datasets during and/or analyzed during the current study are available from the corresponding author on reasonable request.

Competing interests

All authors declare no competing interests.

Funding

The work was supported by the Marquette University College of Engineering GHR Foundation grant, Marquette University startup grant, and Medical College of Wisconsin Department of Surgery We Care grant.

Authors' contributions

BY, TL and TD designed and constructed the DUV-FSM system. MP procured the breast tissue samples and provided the H&E slides and images. AE, RF and TL transported the samples from the Tissue Bank to the research lab. TL stained, imaged and processed the tissues. JMJ provided pathological diagnosis of the samples and training for visual inspection. TGS and DHY provided support on image processing. TGS, DHY and AE provided visual inspection of the tissue samples. BY, TL and TY drafted the manuscript. All authors read and approved the final manuscript.

Acknowledgements

The de-identified human breast tissue specimens were provided by the Medical College of Wisconsin Tissue Bank. The statistical analysis was performed by the Biostatistics Consulting Services (Ulrich Kemmo Tsafack and Dr. Aniko Szabo) at the Medical College of Wisconsin.

References

1. Kummerow, K.L., L. Du, D.F. Penson, Y. Shyr, and M.A. Hooks, *Nationwide trends in mastectomy for early-stage breast cancer*, JAMA Surg, 2015. **150**(1): p. 9-16.
2. Kantor, O., C. Pesce, K. Kopkash, E. Barrera, D.J. Winchester, K. Kuchta, and K. Yao, *Impact of the Society of Surgical Oncology-American Society for Radiation Oncology Margin Guidelines on Breast-Conserving Surgery and Mastectomy Trends*, J Am Coll Surg, 2019.
3. Marinovich, M.L., L. Azizi, P. Macaskill, L. Irwig, M. Morrow, L.J. Solin, and N. Houssami, *The Association of Surgical Margins and Local Recurrence in Women with Ductal Carcinoma In Situ Treated with Breast-Conserving Therapy: A Meta-Analysis*, Ann Surg Oncol, 2016. **23**(12): p. 3811-3821.
4. Donker, M., S. Litiere, G. Werutsky, J.P. Julien, I.S. Fentiman, R. Agresti, P. Rouanet, C.T. de Lara, H. Bartelink, N. Duez, E.J. Rutgers, and N. Bijker, *Breast-conserving treatment with or without radiotherapy in ductal carcinoma In Situ: 15-year recurrence rates and outcome after a recurrence, from the EORTC 10853 randomized phase III trial*, J Clin Oncol, 2013. **31**(32): p. 4054-9.
5. Houssami, N., P. Macaskill, M.L. Marinovich, and M. Morrow, *The association of surgical margins and local recurrence in women with early-stage invasive breast cancer treated with breast-conserving therapy: a meta-analysis*, Ann Surg Oncol, 2014. **21**(3): p. 717-30.
6. Olsen, M.A., K.B. Nickel, J.A. Margenthaler, A.E. Wallace, D. Mines, J.P. Miller, V.J. Fraser, and D.K. Warren, *Increased Risk of Surgical Site Infection Among Breast-Conserving Surgery Re-excisions*, Ann Surg Oncol, 2015. **22**(6): p. 2003-9.
7. Greenup, R.A., J. Peppercorn, M. Worni, and E.S. Hwang, *Cost implications of the SSO-ASTRO consensus guideline on margins for breast-conserving surgery with whole breast irradiation in stage I and II invasive breast cancer*, Ann Surg Oncol, 2014. **21**(5): p. 1512-4.
8. Kaczmarek, K., P. Wang, R. Gilmore, H.N. Overton, D.M. Euhus, L.K. Jacobs, M. Habibi, M. Camp, M.J. Weiss, and M.A. Makary, *Surgeon Re-Excision Rates after Breast-Conserving Surgery: A Measure of Low-Value Care*, J Am Coll Surg, 2019. **228**(4): p. 504-512 e2.
9. Schulman, A.M., J.A. Mirrieles, G. Levenson, J. Landercasper, C. Greenberg, and L.G. Wilke, *Reexcision Surgery for Breast Cancer: An Analysis of the American Society of Breast Surgeons (ASBrS) Mastery(SM) Database Following the SSO-ASTRO "No Ink on Tumor" Guidelines*, Ann Surg Oncol, 2017. **24**(1): p. 52-58.
10. Morrow, M., P. Abrahamse, T.P. Hofer, K.C. Ward, A.S. Hamilton, A.W. Kurian, S.J. Katz, and R. Jagsi, *Trends in Reoperation After Initial Lumpectomy for Breast Cancer: Addressing Overtreatment in*

Surgical Management, JAMA Oncol, 2017. **3**(10): p. 1352-1357.

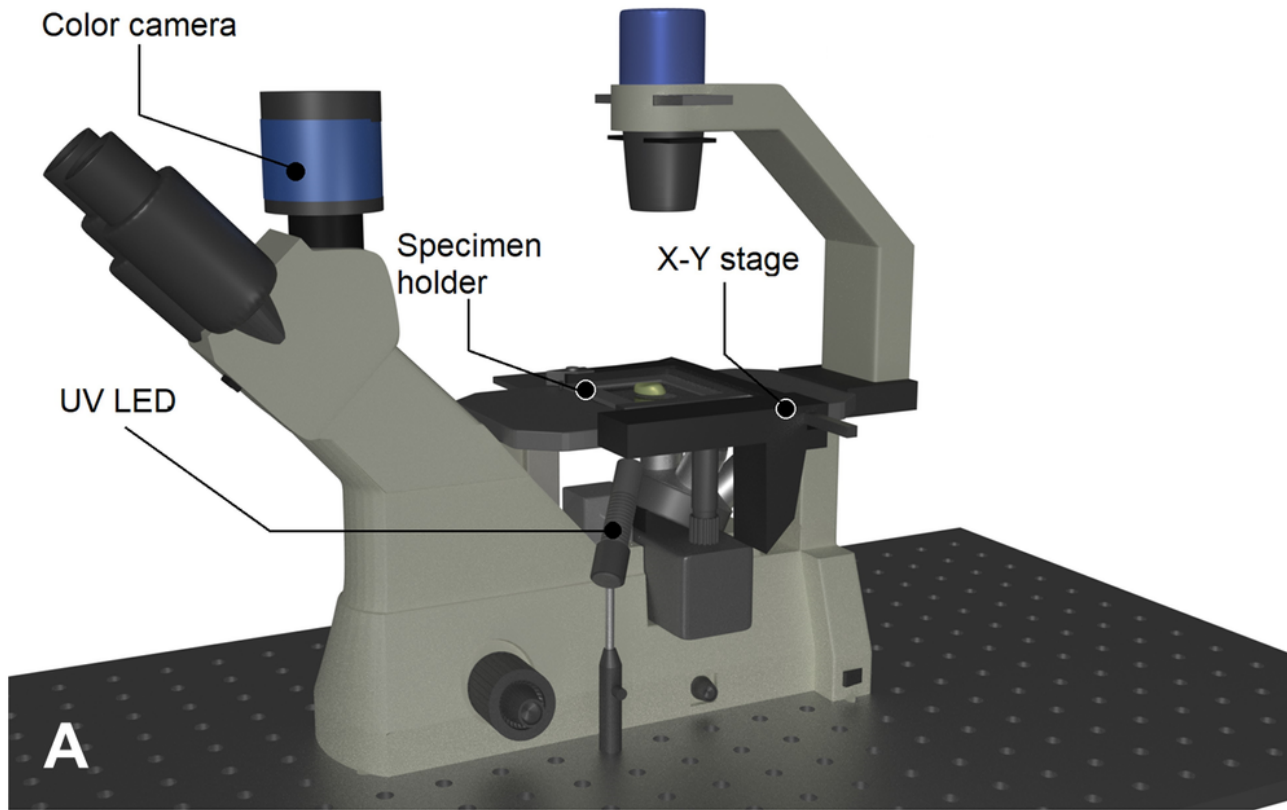
11. Havel, L., H. Naik, L. Ramirez, M. Morrow, and J. Landercasper, *Impact of the SSO-ASTRO Margin Guideline on Rates of Re-excision After Lumpectomy for Breast Cancer: A Meta-analysis*, Ann Surg Oncol, 2019. **26**(5): p. 1238-1244.
12. Graham, R.A., M.J. Homer, C.J. Sigler, H. Safaii, C.H. Schmid, D.J. Marchant, and T.J. Smith, *The efficacy of specimen radiography in evaluating the surgical margins of impalpable breast carcinoma*, AJR Am J Roentgenol, 1994. **162**(1): p. 33-6.
13. St John, E.R., R. Al-Khudairi, H. Ashrafian, T. Athanasiou, Z. Takats, D.J. Hadjiminas, A. Darzi, and D.R. Leff, *Diagnostic Accuracy of Intraoperative Techniques for Margin Assessment in Breast Cancer Surgery: A Meta-analysis*, Ann Surg, 2017. **265**(2): p. 300-310.
14. Park, K.U., H.M. Kuerer, G.M. Rauch, J.W.T. Leung, A.A. Sahin, W. Wei, Y. Li, and D.M. Black, *Digital Breast Tomosynthesis for Intraoperative Margin Assessment during Breast-Conserving Surgery*, Ann Surg Oncol, 2019. **26**(6): p. 1720-1728.
15. Amer, H.A., F. Schmitzberger, B. Ingold-Heppner, J. Kussmaul, M.F. El Tohamy, H.I. Tantawy, B. Hamm, M. Makowski, and E.M. Fallenberg, *Digital breast tomosynthesis versus full-field digital mammography-Which modality provides more accurate prediction of margin status in specimen radiography?*, Eur J Radiol, 2017. **93**: p. 258-264.
16. Olson, T.P., J. Harter, A. Munoz, D.M. Mahvi, and T. Breslin, *Frozen section analysis for intraoperative margin assessment during breast-conserving surgery results in low rates of re-excision and local recurrence*, Ann Surg Oncol, 2007. **14**(10): p. 2953-60.
17. Keating, J.J., C. Fisher, R. Batiste, and S. Singhal, *Advances in Intraoperative Margin Assessment for Breast Cancer*, Curr Surg Rep, 2016. **4**(15).
18. Gray, R.J., B.A. Pockaj, E. Garvey, and S. Blair, *Intraoperative Margin Management in Breast-Conserving Surgery: A Systematic Review of the Literature*, Ann Surg Oncol, 2018. **25**(1): p. 18-27.
19. Schnabel, F., S.K. Boolbol, M. Gittleman, T. Karni, L. Tafra, S. Feldman, A. Police, N.B. Friedman, S. Karlan, D. Holmes, S.C. Willey, M. Carmon, K. Fernandez, S. Akbari, J. Harness, L. Guerra, T. Frazier, K. Lane, R.M. Simmons, A. Estabrook, and T. Allweis, *A randomized prospective study of lumpectomy margin assessment with use of MarginProbe in patients with nonpalpable breast malignancies*, Ann Surg Oncol, 2014. **21**(5): p. 1589-95.
20. Nguyen, F.T., A.M. Zysk, E.J. Chaney, J.G. Kotynek, U.J. Oliphant, F.J. Bellafiore, K.M. Rowland, P.A. Johnson, and S.A. Boppart, *Intraoperative evaluation of breast tumor margins with optical coherence tomography*, Cancer Res, 2009. **69**(22): p. 8790-6.
21. Zysk, A.M., K. Chen, E. Gabrielson, L. Tafra, E.A. May Gonzalez, J.K. Canner, E.B. Schneider, A.J. Cittadine, P. Scott Carney, S.A. Boppart, K. Tsuchiya, K. Sawyer, and L.K. Jacobs, *Intraoperative Assessment of Final Margins with a Handheld Optical Imaging Probe During Breast-Conserving Surgery May Reduce the Reoperation Rate: Results of a Multicenter Study*, Ann Surg Oncol, 2015. **22**(10): p. 3356-62.

22. Zhou, C., D.W. Cohen, Y. Wang, H.C. Lee, A.E. Mondelblatt, T.H. Tsai, A.D. Aguirre, J.G. Fujimoto, and J.L. Connolly, *Integrated optical coherence tomography and microscopy for ex vivo multiscale evaluation of human breast tissues*, Cancer Res, 2010. **70**(24): p. 10071-9.
23. Kennedy, B.F., R.A. McLaughlin, K.M. Kennedy, L. Chin, P. Wijesinghe, A. Curatolo, A. Tien, M. Ronald, B. Latham, C.M. Saunders, and D.D. Sampson, *Investigation of Optical Coherence Microelastography as a Method to Visualize Cancers in Human Breast Tissue*, Cancer Res, 2015. **75**(16): p. 3236-45.
24. Nichols, B.S., C.E. Schindler, J.Q. Brown, L.G. Wilke, C.S. Mulvey, M.S. Krieger, J. Gallagher, J. Geradts, R.A. Greenup, J.A. Von Windheim, and N. Ramanujam, *A Quantitative Diffuse Reflectance Imaging (QDRI) System for Comprehensive Surveillance of the Morphological Landscape in Breast Tumor Margins*, PLoS One, 2015. **10**(6): p. e0127525.
25. Yu, B. and N. Ramanujam, *Quantitative Diffuse Reflectance Imaging of Tumor Margins*, in *Biomedical Photonics Handbook, 2nd Edition*, T. Vo-Dinh, Editor. 2015, CRC Press.
26. Brown, J.Q., T.M. Bydlon, L.M. Richards, B. Yu, S.A. Kennedy, J. Geradts, L.G. Wilke, M. Junker, J. Gallagher, and N. Ramanujam, *Optical Assessment of Tumor Resection Margins in the Breast*, IEEE Journal of Selected Topics on Quantum Electronics, 2010: p., 16:530-544.
27. Keller, M.D., S.K. Majumder, M.C. Kelley, I.M. Meszoely, F.I. Boulos, G.M. Olivares, and A. Mahadevan-Jansen, *Autofluorescence and diffuse reflectance spectroscopy and spectral imaging for breast surgical margin analysis*, Lasers Surg Med, 2010. **42**(1): p. 15-23.
28. Keller, M.D., E. Vargis, N. de Matos Granja, R.H. Wilson, M.A. Mycek, M.C. Kelley, and A. Mahadevan-Jansen, *Development of a spatially offset Raman spectroscopy probe for breast tumor surgical margin evaluation*, J Biomed Opt, 2011. **16**(7): p. 077006.
29. Li, R., P. Wang, L. Lan, F.P. Lloyd, Jr., C.J. Goergen, S. Chen, and J.X. Cheng, *Assessing breast tumor margin by multispectral photoacoustic tomography*, Biomed Opt Express, 2015. **6**(4): p. 1273-81.
30. Wong, T.T.W., R. Zhang, P. Hai, C. Zhang, M.A. Pleitez, R.L. Aft, D.V. Novack, and L.V. Wang, *Fast label-free multilayered histology-like imaging of human breast cancer by photoacoustic microscopy*, Sci Adv, 2017. **3**(5): p. e1602168.
31. Xi, L., S.R. Grobmyer, L. Wu, R. Chen, G. Zhou, L.G. Gutwein, J. Sun, W. Liao, Q. Zhou, H. Xie, and H. Jiang, *Evaluation of breast tumor margins in vivo with intraoperative photoacoustic imaging*, Opt Express, 2012. **20**(8): p. 8726-31.
32. Patel, R., A. Khan, D. Wirth, M. Kamionek, D. Kandil, R. Quinlan, and A.N. Yaroslavsky, *Multimodal optical imaging for detecting breast cancer*, J Biomed Opt, 2012. **17**(6): p. 066008.
33. Tummers, Q.R., F.P. Verbeek, B.E. Schaafsma, M.C. Boonstra, J.R. van der Vorst, G.J. Liefers, C.J. van de Velde, J.V. Frangioni, and A.L. Vahrmeijer, *Real-time intraoperative detection of breast cancer using near-infrared fluorescence imaging and Methylene Blue*, Eur J Surg Oncol, 2014. **40**(7): p. 850-8.
34. Mazhar, A., S. Dell, D.J. Cuccia, S. Gioux, A.J. Durkin, J.V. Frangioni, and B.J. Tromberg, *Wavelength optimization for rapid chromophore mapping using spatial frequency domain imaging*, J Biomed Opt, 2010. **15**(6): p. 061716.

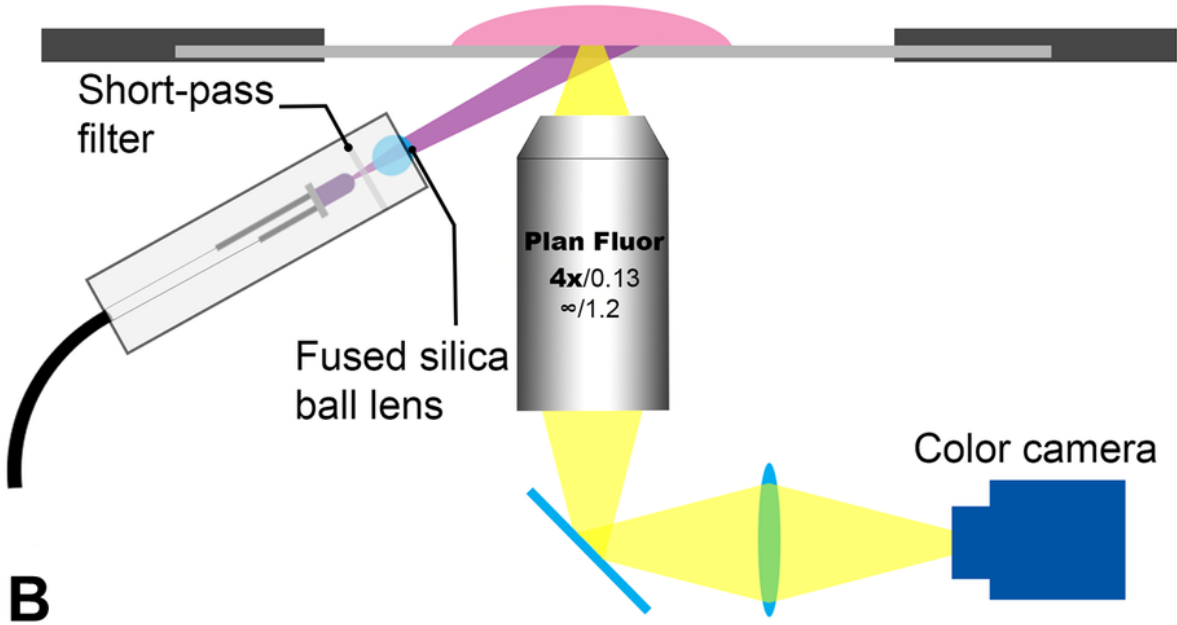
35. Laughney, A.M., V. Krishnaswamy, E.J. Rizzo, M.C. Schwab, R.J. Barth, Jr., D.J. Cuccia, B.J. Tromberg, K.D. Paulsen, B.W. Pogue, and W.A. Wells, *Spectral discrimination of breast pathologies in situ using spatial frequency domain imaging*, Breast Cancer Res, 2013. **15**(4): p. R61.
36. Dixon, J.M., L. Renshaw, O. Young, D. Kulkarni, T. Saleem, M. Sarfaty, R. Sreenivasan, C. Kusnick, J. Thomas, and L.J. Williams, *Intra-operative assessment of excised breast tumour margins using ClearEdge imaging device*, Eur J Surg Oncol, 2016. **42**(12): p. 1834-1840.
37. St John, E., M. Rossi, J. Balog, J. McKenzie, L. Muirhead, A. Speller, L. Gildea, K. Veselkov, S. Shousha, R. Ramakrishnan, Z. Takats, A. Darzi, and D. Leff, *Real time intraoperative classification of breast tissue with the intelligent knife*, European Journal of Surgical Oncology, 2016. **42**(5): p. S25.
38. Glaser, A.K., N.P. Reder, Y. Chen, E.F. McCarty, C. Yin, L. Wei, Y. Wang, L.D. True, and J.T.C. Liu, *Light-sheet microscopy for slide-free non-destructive pathology of large clinical specimens*, Nat Biomed Eng, 2017. **1**(7).
39. Chen, Y., W. Xie, A.K. Glaser, N.P. Reder, C. Mao, S.M. Dintzis, J.C. Vaughan, and J.T.C. Liu, *Rapid pathology of lumpectomy margins with open-top light-sheet (OTLS) microscopy*, Biomed Opt Express, 2019. **10**(3): p. 1257-1272.
40. Maloney, B.W., D.M. McClatchy, B.W. Pogue, K.D. Paulsen, W.A. Wells, and R.J. Barth, *Review of methods for intraoperative margin detection for breast conserving surgery*, J Biomed Opt, 2018. **23**(10): p. 1-19.
41. Dumitru, D., M. Douek, and J.R. Benson, *Novel techniques for intraoperative assessment of margin involvement*, Ecancermedalscience, 2018. **12**: p. 795.
42. Fereidouni, F., Z.T. Harmany, M. Tian, A. Todd, J.A. Kintner, J.D. McPherson, A.D. Borowsky, J. Bishop, M. Lechpammer, S.G. Demos, and R. Levenson, *Microscopy with ultraviolet surface excitation for rapid slide-free histology*, Nat Biomed Eng, 2017. **1**(12): p. 957-966.
43. Yoshitake, T., M.G. Giacomelli, L.M. Quintana, H. Vardeh, L.C. Cahill, B.E. Faulkner-Jones, J.L. Connolly, D. Do, and J.G. Fujimoto, *Rapid histopathological imaging of skin and breast cancer surgical specimens using immersion microscopy with ultraviolet surface excitation*, Sci Rep, 2018. **8**(1): p. 4476.
44. Xie, W., Y. Chen, Y. Wang, L. Wei, C. Yin, A.K. Glaser, M.E. Fauver, E.J. Seibel, S.M. Dintzis, J.C. Vaughan, N.P. Reder, and J.T.C. Liu, *Microscopy with ultraviolet surface excitation for wide-area pathology of breast surgical margins*, J Biomed Opt, 2019. **24**(2): p. 1-11.
45. Peng, T., K. Thorn, T. Schroeder, L. Wang, F.J. Theis, C. Marr, and N. Navab, *A BaSiC tool for background and shading correction of optical microscopy images*, Nat Commun, 2017. **8**: p. 14836.
46. Preibisch, S., S. Saalfeld, and P. Tomancak, *Globally optimal stitching of tiled 3D microscopic image acquisitions*, Bioinformatics, 2009. **25**(11): p. 1463-5.
47. Wu, X., G. Chen, J. Lu, W. Zhu, J. Qiu, J. Chen, S. Xie, S. Zhuo, and J. Yan, *Label-free detection of breast masses using multiphoton microscopy*, PLoS One, 2013. **8**(6): p. e65933.
48. Saad, R.S. and J.F. Silverman, *CHAPTER 25 - Breast*, in *Comprehensive Cytopathology (Third Edition)*, M. Bibbo and D. Wilbur, Editors. 2008, W.B. Saunders: Edinburgh. p. 713-772.

49. Gonzalez, R.C. and E. Richard, *Woods, digital image processing*, ed: Prentice Hall Press, ISBN 0-201-18075, 2002. **8**.
50. Liang, K.-Y. and S.L. Zeger, *Longitudinal data analysis using generalized linear models*, Biometrika, 1986. **73**(1): p. 13-22.
51. Kotwall, C., M. Ranson, A. Stiles, and M.S. Hamann, *Relationship between initial margin status for invasive breast cancer and residual carcinoma after re-excision*, Am Surg, 2007. **73**(4): p. 337-43.
52. Morrow, M., K.J. Van Zee, L.J. Solin, N. Houssami, M. Chavez-MacGregor, J.R. Harris, J. Horton, S. Hwang, P.L. Johnson, M.L. Marinovich, S.J. Schnitt, I. Wapnir, and M.S. Moran, *Society of Surgical Oncology-American Society for Radiation Oncology-American Society of Clinical Oncology Consensus Guideline on Margins for Breast-Conserving Surgery with Whole-Breast Irradiation in Ductal Carcinoma In Situ*, Ann Surg Oncol, 2016. **23**(12): p. 3801-3810.
53. Tadros, A.B., B.D. Smith, Y. Shen, H. Lin, S. Krishnamurthy, A. Lucci, C.H. Barcenas, R.F. Hwang, G. Rauch, L. Santiago, E.A. Strom, S.M. DeSnyder, W.T. Yang, D.M. Black, C.T. Albarracin, M. Chavez-MacGregor, K.K. Hunt, and H.M. Kuerer, *Ductal Carcinoma In Situ and Margins <2 mm: Contemporary Outcomes With Breast Conservation*, Ann Surg, 2019. **269**(1): p. 150-157.
54. Van Zee, K.J., P. Subhedar, C. Olcese, S. Patil, and M. Morrow, *Relationship Between Margin Width and Recurrence of Ductal Carcinoma In Situ: Analysis of 2996 Women Treated With Breast-conserving Surgery for 30 Years*, Ann Surg, 2015. **262**(4): p. 623-31.

Figures



A



B

Figure 1

The DUV-FSM margin imaging system: (A) Principle schematic of the system and (B) The simplified imaging light path. A 45 mW, 285 nm LED with a short-pass filter and a fused silica ball lens has been added to the inverted fluorescence microscope for fluorescence excitation. Fluorescence emission is collected by a Plan Fluor 4x (numerical aperture = 0.13) objective. The excitation/emission filter block of

the microscope is switched to the empty position. Large specimen mosaic scanning is achieved by a motorized XY stage.

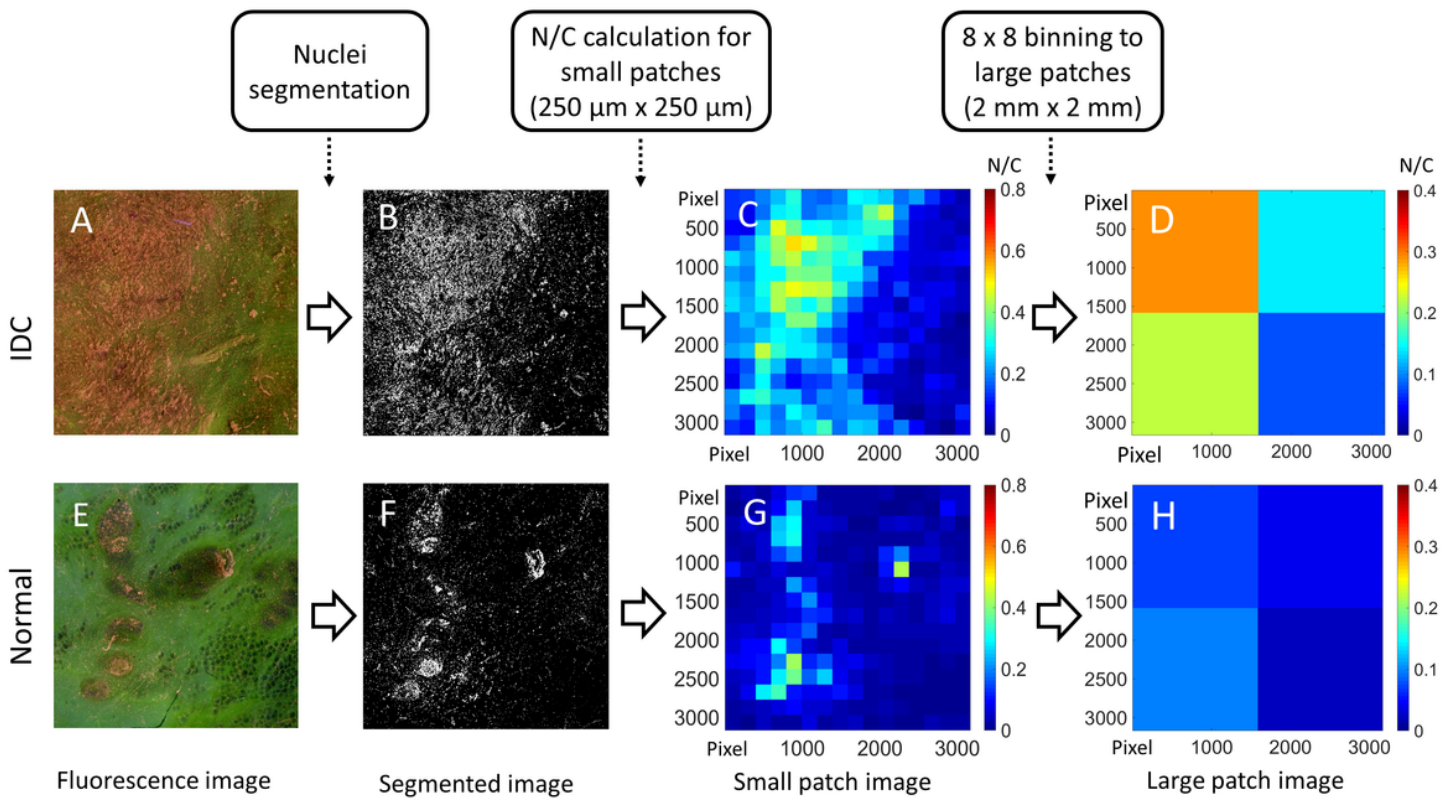


Figure 2

Demonstration of N/C calculation process with an IDC (A-D) and a normal sample (E-H). (A&E) A 4 mm x 4 mm area from the fluorescence images of an IDC and a normal sample, respectively. (B&F) The binarized image after nuclei segmentation from the same region as in (A&E). (C&G) The N/C image calculated with small patches (250 μm x 250 μm). (D&H) 8 x 8 small patches in (C&G) are binned to form large patches (2 mm x 2 mm).

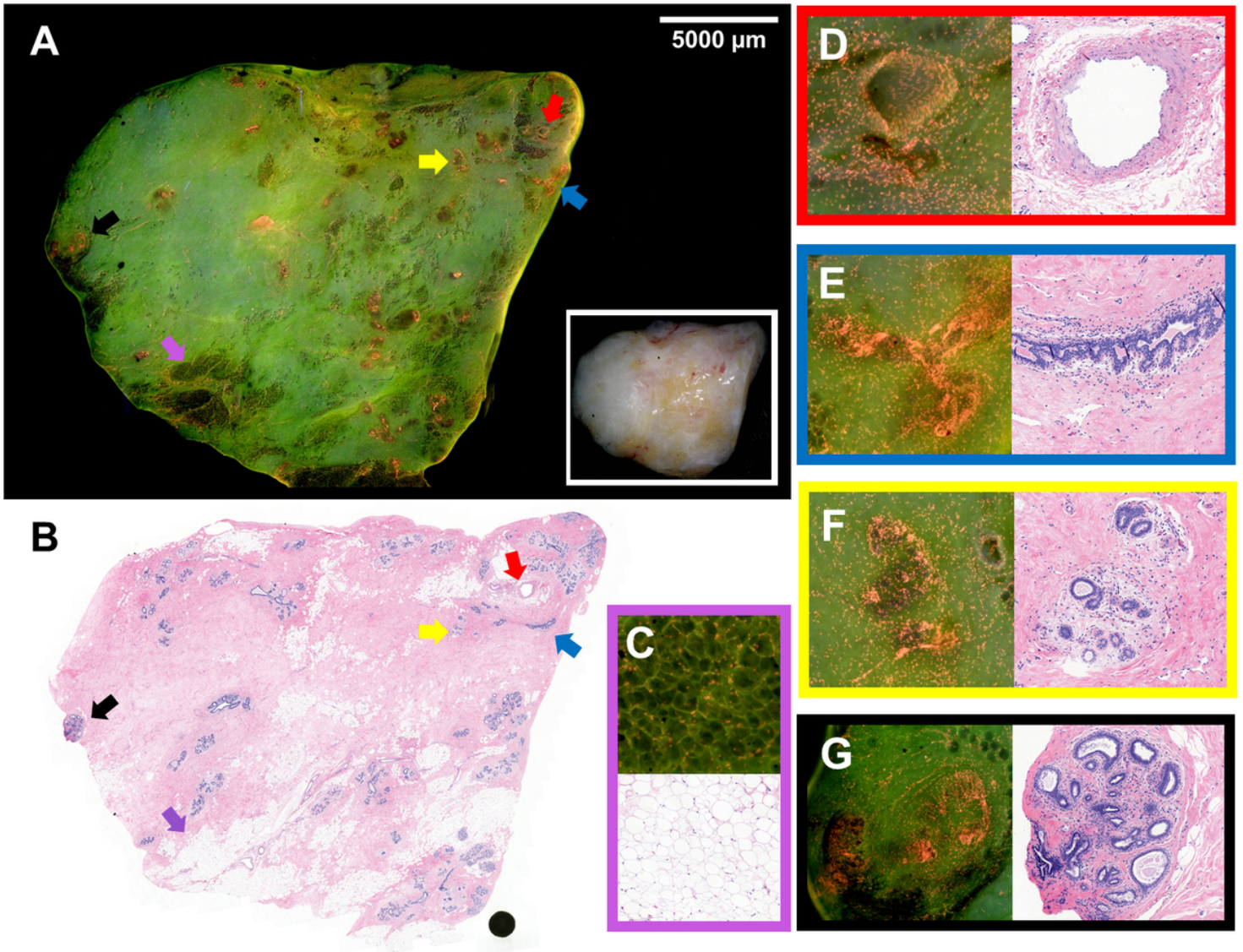


Figure 3

Normal human breast tissue. The fluorescence image (A) of a sample (21 mm x 21 mm) of benign breast glands with interspersed fibroadipose tissue stroma with the specimen photo in the white box and corresponding FFPE H&E image (B). The fluorescence images and corresponding H&E images are shown for (C) adipocytes, (D) muscular-walled blood vessel indicated by the red arrow, (E) duct indicated by the blue arrow, (F) small lobule indicated by the yellow arrow, and (G) lobule with mild adenosis and dilated glands indicated by the black arrow.

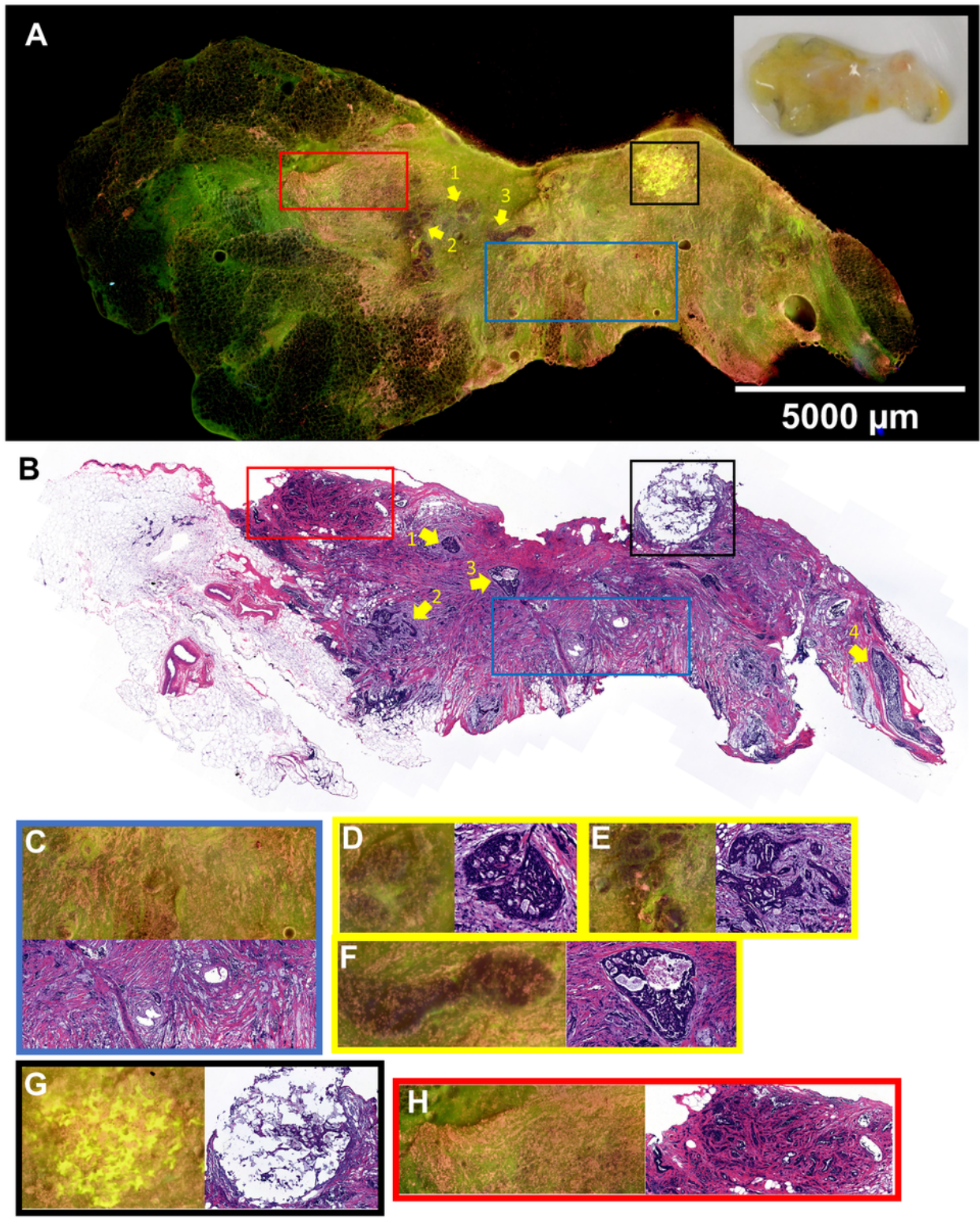


Figure 4

Human breast tissue with ILC and DCIS. (A) The fluorescence image of an ILC sample (20 mm x 10 mm) with adjacent adipose tissue at the two ends. A specimen photo is presented in the white box. (B) FFPE H&E image of the same sample. (C) ILC highlighted by the blue box. Infiltrating single cells and files of cells are evidently visible in the fluorescence image. (D-F) DCIS sites pointed by arrows 1, 2, 3, respectively. The DCIS indicated by arrow 4 is not visible in the fluorescence image, likely because it is

slightly below the surface. (G) Biopsy site highlighted by the black box. A biopsy site usually forecasts abnormalities within the site or nearby. (H) Benign adenosis highlighted by the red box.

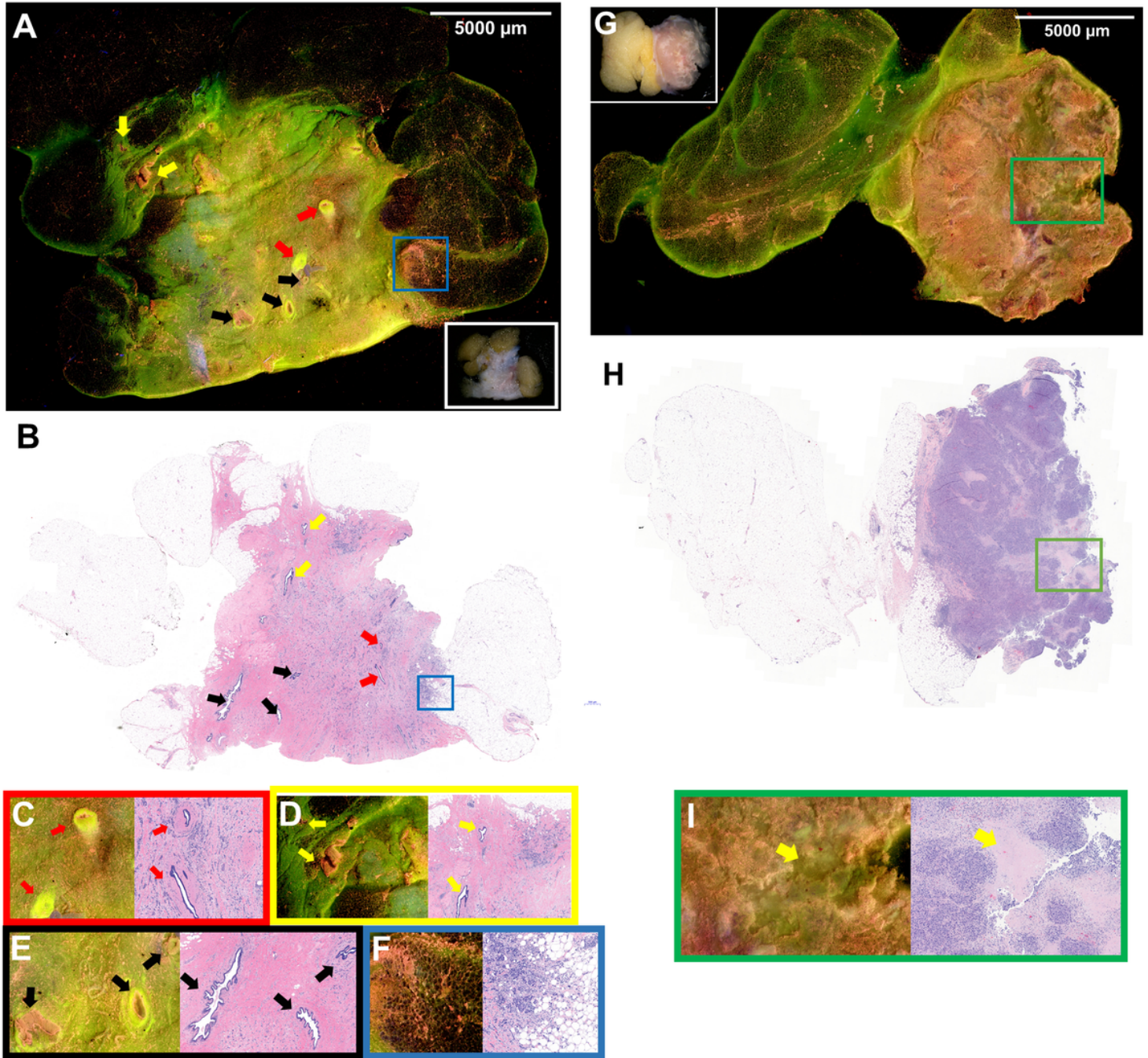


Figure 5

Human breast tissues with IDC. (A) The fluorescence image of an IDC sample (25 mm x 18 mm) with 3-sides surrounded by adipose tissues. The specimen photo is presented in the white box. (B) The FFPE H&E image of the same sample. Benign ducts are indicated by red, yellow and black arrows from different sites and their UV and H&E images are shown in (C), (D) and (E), respectively. The tumor site with higher nuclear density at the interface between fibrotic stroma and adipose tissue in the blue box is shown in (F). (G) The fluorescence image of a high-grade IDC sample (25 mm x 17 mm) with necrosis

and the specimen photo in the white box. (H) FFPE H&E image of the same sample. The region in the red box is exhibited in (I) with the necrosis sites indicated by the yellow arrows.

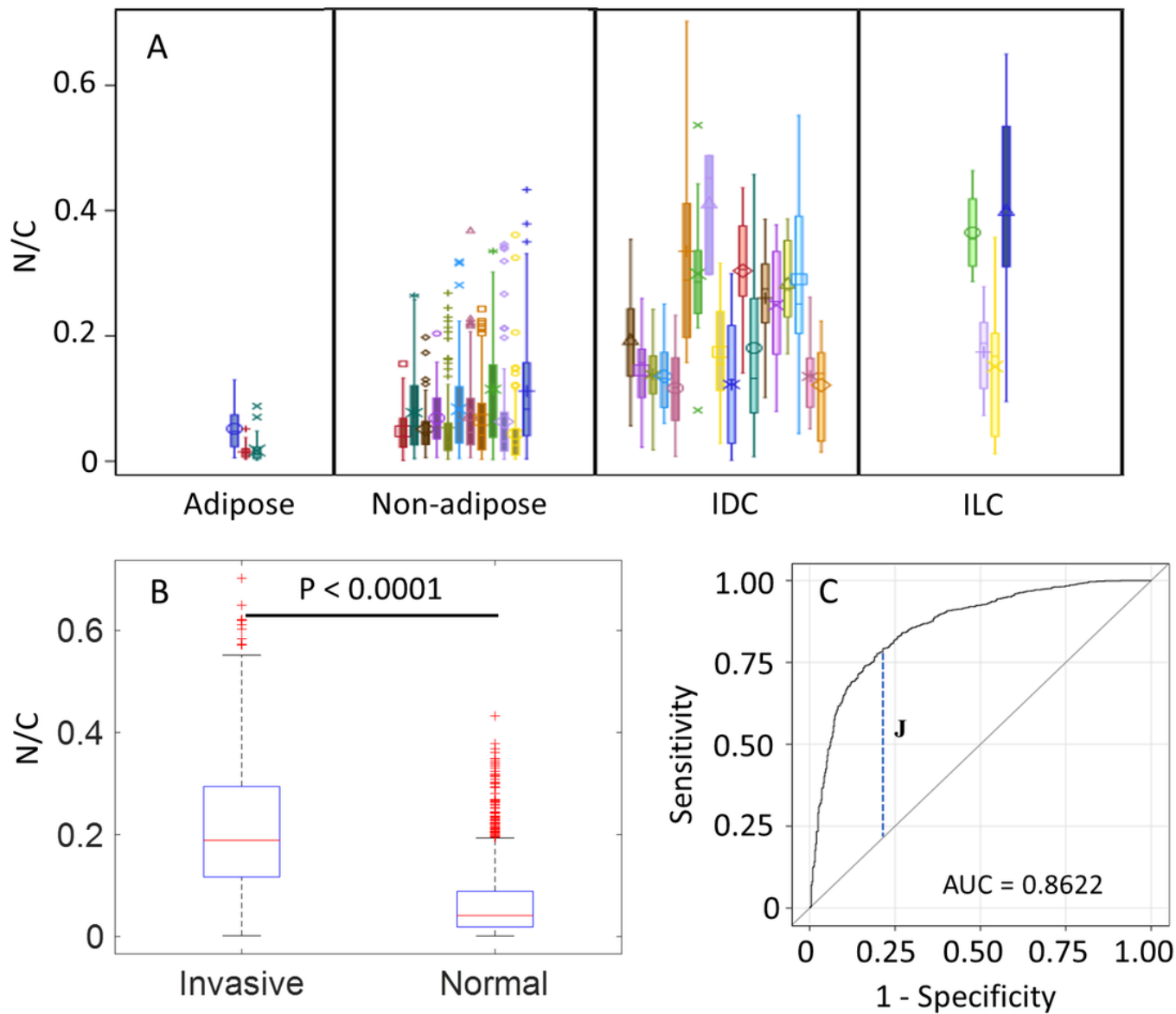


Figure 6

Results of statistical comparison and classification. (A) The boxplot of N/C by specimen subtype (adipose-rich, non-adipose-rich normal, IDC and ILC). (B) The boxplot of two-class classification. Outliers are represented by red crosses in (B). (C) ROC curve for classifying patch-level normal and invasive tissue. J is the Youden's index.